Automatic Retinal Layer Segmentation of OCT Images With Central Serous Retinopathy

Dehui Xiang, Geng Chen, Fei Shi, Weifang Zhu, Qinghuai Liu, Songtao Yuan, and Xinjian Chen

***Abstract*—In this paper, an automatic method is reported for simultaneously segmenting layers and fluid in 3-D OCT retinal images of subjects suffering from central serous retinopathy. To enhance contrast between adjacent layers, multiscale bright and dark layer detection filters are proposed. Due to appearance of serous fluid or pigment epithelial detachment caused fluid, contrast between adjacent layers is often reduced, and also large morphological changes are caused. In addition, 24 features are designed for random forest classifiers. Then, 8 coarse surfaces are obtained based on the trained random forest classifiers. Finally, a hypergraph is constructed based on the smoothed image and the layer structure detection responses. A modified live wire algorithm is proposed to accurately detect surfaces between retinal layers, even though OCT images with fluids are of low contrast and layers are largely deformed. The proposed method was evaluated on 48 spectral domain OCT images with central serous retinopathy. The experimental results showed that the proposed method outperformed the state-of-art methods with regard to layers and fluid segmentation.**

***Index Terms*—Central serous retinopathy, optical coherence tomography, random forest, hybrid live wire.**

I. Introduction

CENTRAL serous retinopathy (CSR) is a serious complex disease that usually leads to blindness. CSR occurs due to accumulation of serous fluid under interdigitation zone [1] of retina and may also lead to retinal pigment epithelium detachment, as shown in Fig. 1. There are two types of CSR [2], [3]. In Type 1 CSR, only serous fluid accumulates under the interdigitation zone. In Type 2 CSR, retinal pigment epithelium detachment may appear under serous fluid and may also occur near the center of the macula. The two types of fluid lead to large morphological changes of retinal layers. In addition, thickness and optical intensity of retinal layers may change abruptly due to occurrence of CSR [4]–[6]. CSR is one common type of macular disorders and the macula is responsible for the central vision. It is important to provide accurate diagnosis and treatment of CSR.

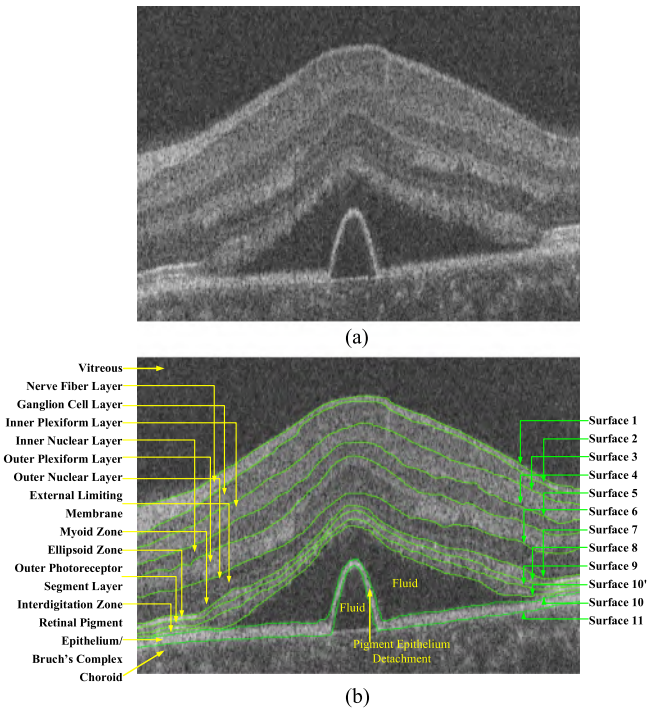

Fig. 1. OCT image with central serous retinopathy. (a) A B-scan image of OCT volume; (b) The manual annotation of retinal surfaces and layers.

Optical coherence tomography (OCT) is a noninvasive and non-contact imaging modality for morphological analysis and diagnosis of retinal abnormality, such as CSR, macular hole, diabetic macular edema, glaucoma and age-related macular degeneration. The great improvements of OCT devices make it possible diagnose and monitor retinal diseases more accurately. Layer and lesion segmentation are basic steps for abnormality quantification. Fig. 1 shows a macular centered OCT B-scan image with CSR. The vitreous, retina, fluid and choroid are annotated with arrows. The surfaces are numbered 1 to 11 from top to bottom. The retinal layers are nerve fiber layer (NFL), ganglion cell layer (GCL), inner plexiform layer (IPL), inner nuclear layer (INL), outer plexiform layer (OPL), outer

Manuscript received July 3, 2017; revised August 28, 2017 and January 5, 2018; accepted January 30, 2018. Date of publication February 7, 2018; date of current version January 2, 2019. This work was supported in part by the National Basic Research Program of China (973 Program) under Grant 2014CB748600, in part by the National Natural Science Foundation of China under Grant 81371629, Grant 61401293, Grant 61401294, Grant 81401451, and Grant 81401472, and in part by the Graduate Student Scientific Research Innovation Project of Jiangsu Province in China under Grant SJCX17_0650. *(Corresponding authors: Xinjian Chen and Dehui Xiang.)*

D. Xiang, G. Chen, F. Shi, W. Zhu, and X. Chen are with the School of Electronics and Information Engineering, and with the State Key Laboratory of Radiation Medicine and Protection, School of Radiation Medicine and Protection, Soochow University, Suzhou 215006, China (e-mail: xiangdehui@suda.edu.cn; xjchen@suda.edu.cn; chengeng@suda.edu.cn; shifei@suda.edu.cn; wfzhu@suda.edu.cn).

Q. Liu and S. Yuan are with the Jiangsu Province Hospital, Nanjing 210029, China (e-mail: yuansongtao@vip.sina.com; liuqh0545@126.com).

Digital Object Identifier 10.1109/JBHI.2018.2803063

nuclear layer (ONL), external limiting membrane (ELM), myoid zone, ellipsoid zone, outer photoreceptor segment layer (OPSL), interdigitation zone, retinal pigment epithelium (RPE)/Bruch's complex and choroid. The abnormalities include serosity (fluid), pigment epithelial detachment (PED) caused fluid.

To quantify thickness of retinal layers and volume of fluid,is important to develop a tool for reliable and automatic segmentation of both retinal layers and fluid since manual segmentation is time-consuming for huge amount of OCT images in clinic applications. However, there are several challenges in retinal layer and fluid segmentation. First, internal structures of retinas are complex and difficult to be recognized as shown in Fig. 1. Inner boundaries of retinal layers are non-smooth and retinal layers produce great morphological and structural changes. Second, there may be several types of fluid, e.g., serosity, PED caused fluid. This leads to low contrast and blurred boundaries in OCT images between retinal layers. Therefore, layer segmentation may fail in using traditional surface detection methods, such as the graph search algorithm. Fluid segmentation using conventional methods, such as region growing may easily leak into its neighbors. Therefore, new methods that can segment retinal layers with fluid are needed for quantitative analysis of CSR.

In this paper, we focus on segmentation for retinas with CSR in OCT images, which is associated with serosity and PED caused fluid. A fully automatic, supervised layer segmentation method is proposed for macular-centered OCT images with CSR. Shapes and intensities of retinal layers are learned by random forest classifiers using a weighted voting mechanism proposed in our previous work [7] since each tree contributes unevenly to the final decision depending on the strength of classification for a new example [8]. Layer detection filters are introduced and a hyper graph is constructed for the live wire algorithm to cope with the low contrast and blurred boundaries. The initial surfaces constrain the refinement of retinal surfaces by using the hybrid live wire algorithm so as to cope with the structural changes of retinal layers. Compared to our previous work [9], it is much more difficult to detect surfaces in OCT images with CSR since fluid may exhibit in the retina and below RPE. Compared to previous methods, the novelty of the proposed method lies in:

(1) Multi-scale bright and dark layer-like structure detection filters are designed for estimation of possible bright and dark retinal layers with different thickness since OCT images with fluid are of low contrast and layer boundaries are blurred.
(2) Twenty four features are introduced to random forest classifiers aiming at finding the initial surfaces of retinal layers affected by abnormalities, such as serosity and PED caused fluid, which is different from the boundary based random forest method [10].
(3) A hyper graph is constructed based on the smoothed image and the layer structure detection responses, and then a modified live wire algorithm is proposed to accurately detect surfaces between retinal layers even though retinal layers are deformed due to fluid.
(4) Layer segmentation and abnormal region segmentation are simultaneously performed and the proposed method achieves higher accuracy than previous methods [9], [11].

II. Related Work

Many methods have been proposed for automatic retinal layer segmentation of OCT images. Most methods are based on the graph search algorithm [12]–[19]. Recently, by combining the graph search algorithm and Dijkstra's algorithm, Tian *et al.* [20] proposed a shortest path based graph search to detect retinal boundaries by searching the shortest path between two end nodes. The time complexity was reduced by the limitation of the search region and down-sampling. Vermeer *et al.* [21] used support vector machines with features based on image intensities and gradients to detect five interfaces of retinas. Srinivasan *et al.* [22] also used support vector machines combined with average intensity of each row to find the initial surfaces, and then used the graph theory based dynamic programming algorithm to detect six surfaces in OCT images of wild-type rat retinas. Lang *et al.* [10] introduced a random forest classifier to classify eight retinal layers in macular cube images. The features were mainly designed for boundary classification of the normal eyes since the contrast between neighboring layers was much higher than that of OCT images of abnormal retinas. Novosel *et al.* [23] developed a loosely-coupled level set method to segment retinal layers coupling through the order of layers and thickness priors but only eight interfaces were detected in the OCT images from normal retinas.

Many other methods concentrated on the segmentation of retinal abnormalities. Quellec *et al.* [24] reported an automated symptomatic exudate-associated derangements (SEAD) footprint detection method. Chen *et al.* [11] proposed a graph-search-graph-cut (GSGC) method to segment SEAD associated with AMD. Dufour *et al.* [25] proposed a graph-search algorithm with trained hard and soft constraints to deal with drusen. Ding *et al.* [26] used a graph cut method to segment top and bottom layers of retina and then a split Bregman-based segmentation method was used to segment subretinal fluid and sub-RPE fluid between layers. Finally, a random forest classifier was trained to segment the true fluid regions. In previous work, we proposed a multi-resolution graph search method to perform simultaneous layer segmentation and fluid segmentation. This method is effective for OCT images with serous PEDs [9]. Xu *et al.* [27] developed a voxel classification based approach using a layer-dependent stratified sampling strategy to detect SEAD. Hassan *et al.* [3] used a structure tensor approach combined with a nonlinear diffusion process for the automated detection of ELM and choroid in order to discriminate macular edema and CSR from OCT images using a support vector machine classifier. Wang *et al.* [28] utilized a fuzzy level set-based segmentation method to segment diabetic macular edema. De Sisternes *et al.* [29] segmented nine surfaces from OCT images in normal and age-related macular degeneration eyes based on the iterative adaptation of a weighted median process, which is constrained with a set of smoothness constraints and pre-defined rules. Novosel *et al.* [6] developed a locally-adaptive loosely-coupled level set method to segment retinal layers and fluids in OCT images with CSR. However, only four interfaces and

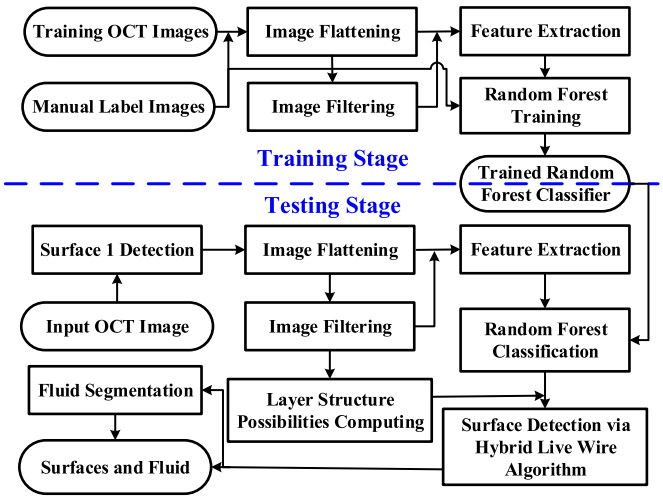

Fig. 2. Flow chart of the proposed framework.

CSR without PED fluids were segmented. Novosel *et al.* [30] used a loosely-coupled level set method again to segment retinal layers and lesions in OCT images with CSR and AMD but only detected seven surfaces in non-vessel regions.

III. Method Overview

The proposed framework can be split into two stages: training stage and testing stage illustrated in Fig. 2. In the training stage, OCT images are manually annotated and features are extracted for random forest classifier training. In the testing stage, the proposed segmentation method is a coarse-to-fine segmentation process that consists of three steps: preprocessing, initialization and segmentation. Original OCT image is preprocessed to reduce noise and gray levels are normalized. The necessary feature vector is computed from preprocessed OCT images and initial surfaces of retinal layer are computed with the application of random forest classifiers to label voxels as different retinal layers. The final surfaces are refined via the proposed hybrid live wire algorithm and fluid is also segmented.

IV. Pre-Processing

A. Surface 1 Detection and Image Flattening

Due to eye movement and delay of OCT imaging, unpredictable displacement between successive B-scan images exists in most volumetric OCT images and cause inaccurate boundary detection. These displacements also lead to image artifacts during the curvature anisotropic diffusion filtering. Image flattening is often employed to correct the irregular displacements [9], [13], [20]. A fast method is proposed to find initial surface 1 for the fine surface detection. Gaussian filtering is used to slice-by-slice smooth B-scan images of the original 3D OCT image to suppress speckle noise.The Canny edge detection algorithm is used to obtain initial surface 1 and a coarse bottom surface between retinal pigment epithelium (RPE)/Bruch's complex and choroid. The single graph live wire algorithm described in Section VI-A is used to detect the clear boundary between vitreous and NFL. After surface 1 is detected, it is considered as

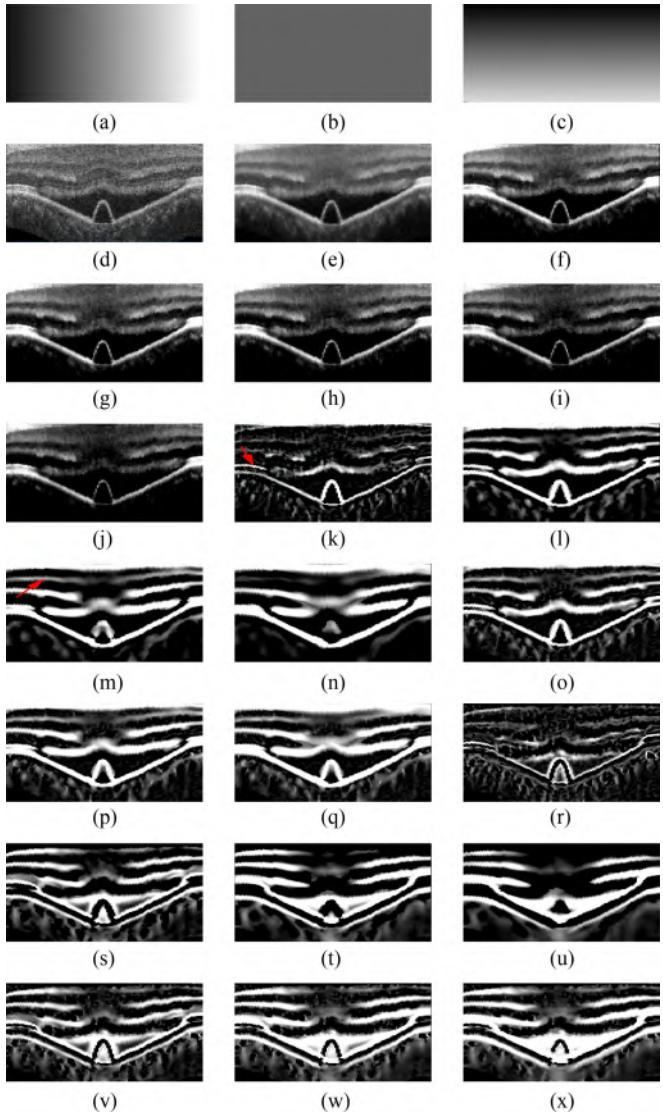

Fig. 3. Classification features. (a)–(c) Three spatial features; (d) The flattened original image; (e) The curvature anisotropic diffusion filtered image; (f)–(j) Five normalized features; (k)–(n) Four single scale bright layer responses ($\sigma_t = 2, 3, 4, 5$); (o)–(q) Three multiple scale bright layer responses($\sigma_{t,\min} = 2, \sigma_{t,\max} = 3, 4, 5$); (r)–(u) Four single scale dark layer responses ($\sigma_t = 2, 3, 4, 5$); (v)–(x) Three multiple scale dark layer respons ($\sigma_{t,\min} = 2, \sigma_{t,\max} = 3, 4, 5$).Ellipsoid zone layer is enhanced when σ_t is set to 2 as pointed by the red arrow in (k). IPL layer is enhanced when σ_t is set to 4 as pointed by the red arrow in (m).

nce plane. Each A-line below surface 1 is top aligned to obtain flattened images such robustness of the proposed framework is improved. The subvolume of the input OCT image between surface 1 and the coarse bottom surface is extracted.

B. Filtering and Contrast Enhancement

An anisotropic diffusion filter is applied to reduce noise [27], [31] since the filter can reduce speckle noise and preserve boundary of retinal layers. As can be seen in Fig. 1(b), intensities of vitreous and choroid are comparative to some retinal layers in OCT image. To reduce the influence of these two Structures, intensities of vitreous and choroid should be

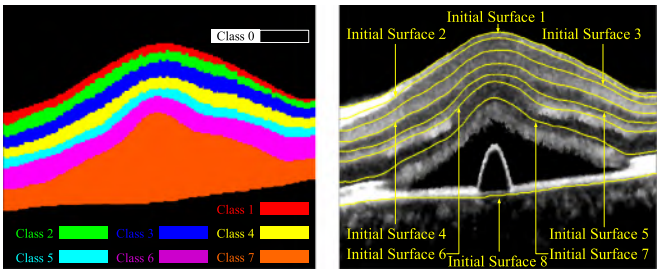

Fig. 4. Automatic surface detection. (a) Voxel classification via random forest; (b) The eight initial curves/surfaces with the filtered image.

ssed. In addition, contrast between adjacent retinal layers can also be enhanced. The filtered and smoothed image is then normalized as,

$$I_N(\vec{x}) = \begin{cases} I_{N,\max}; & I_f(\vec{x}) \geq I_{f,s} + I_{f,r}; \\ \frac{I_{N,\max}}{I_{f,r}}\left(I_f(\vec{x}) - I_{f,s}\right); & I_{f,s} \leq I_f(\vec{x}) < I_{f,s} + I_{f,r}; \\ 0; & I_f(\vec{x}) < I_{f,s}. \end{cases} \tag{1}$$

where $I_f(\vec{x})$ is the intensity of a voxel, $\vec{x}$ denotes 3D coordinates, $I_{f,s}$ denotes the lower intensity, $I_{f,r}$ is the intensity range, $I_{f,s} + I_{f,r}$ is therefore the upper intensity, $I_{N,\max}$ is the output maximal normalized intensity. Intensities of vitreous and choroid are highly reduced as shown in Fig. 4(b).

V. Initial Surface Detection

Since inner boundaries of retinal layers are non-smooth and abnormal retinal layers produce great morphological and structural changes, it is advisable that initial boundaries of retinal layers are detected and used to constrain the fine segmentation. Recently, machine learning classifiers have been introduced into normal layer recognition of ophthalmic OCT images [10], [21]. Vermeer *et al.* [21] defined Haar-like features such as averages and gradients in A-line and B-scan with different scales, and then used the support vector machine to classify pixels. Lang *et al.* [10] also proposed retinal layer boundary based features such as signed value of the first derivative and magnitude of the second derivative, and then used random forest classifiers to segment eight retinal layers. Those two methods mainly used boundary based features to provide a probability of pixels belonging to each layer; however, contrast between two layers is often low and the boundaries are also weak because of the occurrence of the serosity under the ONL.

In this paper, the random forests method based on our previous work [7] is used. The retinal layers in OCT images with CSR are manually labeled as eight classes. Class 1: NFL, Class 2: GCL, Class 3: IPL, Class 4: INL, Class 5: OPL, Class 6: ONL + ELM + myoid zone, Class 7: ellipsoid zone + OPSL + interdigitation zone + RPE/Bruch's complex + fluid, and Class 0: choroid. High-dimensional features and labels are used to train random forest classifiers. Due to high resolutions and large size of OCT images, the number of features is much smaller than that in some previous applications [7], [10]. Due to appearance of serous fluid or PED caused fluid, contrast between adjacent layers is often reduced, and also large morphological changes are caused. In order to reduce this influence of fluid, twenty four features including: layer location, gray scale and structural response are proposed to find initial retinal layers.

A. Layer Location Features

Unlike normal retinal layers, fovea is often deformed upward by fluid in OCT images with CSR. It is impossible to find the center of the fovea by computing the thinnest position as in [10]. Suppose $\bar{I}_f(\vec{x})$ is the flattened and smoothed training or testing 3D OCT image. Coordinates of each voxel are $\vec{x} = x, y, z$. Since $\bar{I}_f(\vec{x})$ is the flattened and smoothed image, surface 1 is considered as the $x - y - 0$ plane. For the image $\bar{I}_f(\vec{x})$, each B-scan image is scanned to obtain x, y and z coordinates of each voxel. Since layers and fluid are located in certain restricted space, these three features ($F_1(\vec{x}) = x, F_2(\vec{x}) = y, F_3(\vec{x}) = z$) denote the location information of each voxel related to the interface of vitreous and NFL, as shown in Fig. 3(a)–(c).

B. Gray Scale Features

The intensity of the flattened original image $I(\vec{x})$ is considered as one feature $F_4(\vec{x}) = \bar{I}(\vec{x})$ as shown in Fig. 3(d). The flattened original image is denoised with the curvature anisotropic diffusion filtering. The intensity of the flattened and smoothed image $\bar{I}_f(\vec{x})$ is considered as one feature $F_5(\vec{x}) = \bar{I}_f(\vec{x})$ as shown in Fig. 3(e). In the clinical images, the intensity range varies from one patient to another and the contrast between neighboring layers is often low. To address these problems, sub-range intensity of $\bar{I}_f(\vec{x})$ is further normalized as,

$$F_i(\vec{x}) = \begin{cases} \bar{I}_{\max}; & \bar{I}_f(\vec{x}) \geq I_{f2}; \\ \frac{\bar{I}_{\max}}{I_{f2} - I_{f1}}\left(\bar{I}_f(\vec{x}) - I_{f1}\right); & I_{f1} \leq \bar{I}_f(\vec{x}) < I_{f2}; \\ 0; & \bar{I}_f(\vec{x}) < I_{f1}. \end{cases} \tag{2}$$

where $F_i(\vec{x})$ is the normalized gray scale feature ($i = 6, 7, \ldots, 10$), I_{f1} denotes the lower intensity, I_{f2} denotes the upper intensity, $\bar{I}_{\max}$ is the output maximal normalized intensity. Five normalized gray scale features are used and allow the classifiers to easily differentiate the darker layers and the brighter layers, and particularly recognize NFL, IPL, OPL, ellipsoid zone + OPSL + interdigitation zone + RPE/Bruch's complex, as shown in Fig. 3(f)–(j).

C. Structural Response Features

Although sub-range intensity normalization is useful to improve the contrast between adjacent layers, structural responses can also provide distinguishable layer features according to layer structures. Since thickness varies from different retinal layers and dark-to-bright or bright-to-dark transition is often kept in OCT images. Therefore, retinal layers with different thickness can be enhanced by layer detection filters with different scales in scale space, and additional features with single scale and

multiple scale layer detection filters can be supplemented to discriminate different layers. For estimation of the possibility of a layer element in a 3D OCT image, Hessian matrix is computed in the scale space as

$$H\left(\vec{x},\sigma_t\right)=\bar{I}_f\left(\vec{x}\right)*\begin{bmatrix}\frac{\partial^2 G(\vec{x},\sigma_t)}{\partial x^2} & \frac{\partial^2 G(\vec{x},\sigma_t)}{\partial x\partial y} & \frac{\partial^2 G(\vec{x},\sigma_t)}{\partial x\partial z}\\ \frac{\partial^2 G(\vec{x},\sigma_t)}{\partial y\partial x} & \frac{\partial^2 G(\vec{x},\sigma_t)}{\partial y^2} & \frac{\partial^2 G(\vec{x},\sigma_t)}{\partial y\partial z}\\ \frac{\partial^2 G(\vec{x},\sigma_t)}{\partial z\partial x} & \frac{\partial^2 G(\vec{x},\sigma_t)}{\partial z\partial y} & \frac{\partial^2 G(\vec{x},\sigma_t)}{\partial z^2}\end{bmatrix} \tag{3}$$

where $*$ denotes the convolution operation, $G\left(\vec{x},\sigma_t\right)$ is a 3D Gaussian function, σ_t is the standard deviation (also called scale). The three eigenvalues of $H\left(\vec{x},\sigma_t\right)$: $\left|\lambda_1\left(\vec{x},\sigma_t\right)\right| \leq \left|\lambda_2\left(\vec{x},\sigma_t\right)\right| \leq \left|\lambda_3\left(\vec{x},\sigma_t\right)\right|$ can be used to define layer structural responses.

For bright layer structures, $\lambda_3\left(\vec{x},\sigma_t\right)<0$ has to be satisfied; while for dark layer structures, $\lambda_3\left(\vec{x},\sigma_t\right)>0$ has to be satisfied. For a bright layer with a certain thickness, structural response most stably corresponds to some specific scale σ_t. Therefore, σ_t can also be considered as the thickness of a layer, and the bright layer possibility can be estimated in the scale space as

$$L\left(\vec{x},\sigma_t\right) = \begin{cases}\left|\lambda_3\left(\vec{x},\sigma_t\right)\right|\exp\left(-\frac{\alpha\lambda_1^2\left(\vec{x},\sigma_t\right)+\beta\lambda_2^2\left(\vec{x},\sigma_t\right)}{\lambda_3^2\left(\vec{x},\sigma_t\right)}\right), & \lambda_3\left(\vec{x},\sigma_t\right)<0\\ 0, & \lambda_3\left(\vec{x},\sigma_t\right)\geq 0\end{cases} \tag{4}$$

where α and β are symmetric parameters, which control the ratio between the two minor components $\lambda_1\left(\vec{x},\sigma_t\right)$, $\lambda_2\left(\vec{x},\sigma_t\right)$ and the principal component $\lambda_3\left(\vec{x},\sigma_t\right)$. With a single scale or thickness σ_t, bright layer structural response feature $F_i\left(\vec{x}\right)=L\left(\vec{x},\sigma_t\right)$ can be computed by (4) $(i=11,12,\ldots,14)$, as shown in Fig. 3(k)–(n). For instance, ellipsoid zone layer is enhanced when σ_t is set to 2 as pointed by the red arrow in Fig. 3(k). IPL layer is enhanced when σ_t is set to 4 as pointed by the red arrow in Fig. 3(m). The dark layer possibility is defined as

$$L\left(\vec{x},\sigma_t\right) = \begin{cases}\left|\lambda_3\left(\vec{x},\sigma_t\right)\right|\exp\left(-\frac{\alpha\lambda_1^2\left(\vec{x},\sigma_t\right)+\beta\lambda_2^2\left(\vec{x},\sigma_t\right)}{\lambda_3^2\left(\vec{x},\sigma_t\right)}\right), & \lambda_3\left(\vec{x},\sigma_t\right)>0\\ 0, & \lambda_3\left(\vec{x},\sigma_t\right)\leq 0\end{cases} \tag{5}$$

Similarly, with a single scale or thickness σ_t, dark layer structural response feature $F_i\left(\vec{x}\right)=L\left(\vec{x},\sigma_t\right)$ can be computed by (5) $(i=18,19,\ldots,21)$ as shown in Fig. 3(r)–(u).

To take into account varying sizes of the layers, the scale-dependent layer possibility function $L\left(\vec{x},\sigma_t\right)$ is computed for all voxels $\vec{x}$ of the 3D image domain. Thickness values are discretized values between a minimal scale $\sigma_{t,\min}$ and a maximal scale $\sigma_{t,\max}$, using a linear scale. The multiscale bright and dark layer response are both obtained by selecting the maximum response over the range of all scales with the corresponding single scale response in (4) and (5) as

$$L_m\left(\vec{x},\sigma_t\right)=\max_{\sigma_{t,\min}\leq\sigma_t\leq\sigma_{t,\max}}\sigma_t^2 L\left(\vec{x},\sigma_t\right) \tag{6}$$

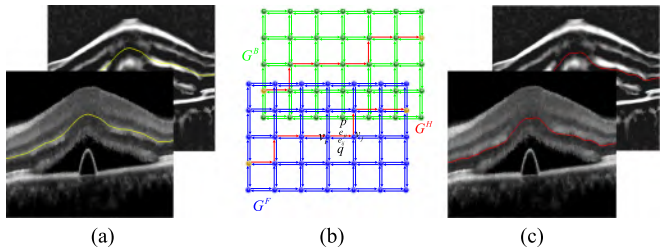

Fig. 5. Hybrid live wire. (a) The bright layer enhanced image and the filtered image with a initial curve (yellow); (b) The hybrid graph G^H; (c) The bright layer enhanced image and the filtered image with the refined curve (red) via the hybrid live wire algorithm.

where m represents the multiscale filtering. Therefore, with multiple scales, bright layer multiscale structural response feature $F_i\left(\vec{x}\right)=L\left(\vec{x},\sigma_t\right)$ can be computed by (6) $(i=15,16,17)$ as shown in Fig. 3(o)–(q). Similarly, dark layer multiscale structural response feature $F_i\left(\vec{x}\right)=L\left(\vec{x},\sigma_t\right)$ can be computed by (6) $(i=22,23,24)$, as shown in Fig. 3(v)–(x).

The bright layer responses allow the classifiers to learn the possibility of NFL, IPL, OPL, ellipsoid zone + OPSL + interdigitation zone + RPE/Bruch's complex while the dark layer responses allow the classifier to learn the possibility of GCL, INL, ONL + ELM + myoid zone and choroid. For each scale, the bright layer responses [Fig. 3(k)–(n)] and the dark responses [Fig. 3(r)–(u)] are computed. Multiple responses from the minimal scale and current scale [Fig. 3(o)–(q) and (v)–(x)] are also computed. Totally, fourteen layer structural response features are generated for the classifier. The eigenvectors of Hessian matrix corresponding to the three eigenvalues $\lambda_1\left(\vec{x},\sigma_t\right),\lambda_2\left(\vec{x},\sigma_t\right),\lambda_3\left(\vec{x},\sigma_t\right)$ are orthogonal to each other. One eigenvector is the normal of the layer and the other two eigenvector are tangent. Therefore, layer response features are robust to the deformation and rotation of retinal layers even with the existence of diseases such as fluid. The random forest classifiers are trained and used to predict the label of each voxel of OCT images as shown in Fig. 4(a). The initial curves/surfaces are shown in Fig. 4(b).

VI. Live Wire for Surface Detection

A. Single Graph Live Wire

1) Single Graph Construction: By following the recommendation in [32], [33] for a 2D image as shown in Fig. 5(b), a single graph (the blue mesh G^F) can be constructed for Surface 1 Detection. Let a connected and directed graph G be represented as a pair $G=(V,E)$ with nodes $v\in V$ and edges $e\in E$. A directed edge e_{ij} connects a node v_i and a neighboring node v_j and points from the node v_i to the node v_j, while e_{ji} denotes the directed edge pointing from the node v_j to the node v_i. The edge e_{ij} is weighted by c_{ij} and the edge e_{ji} is weighted by c_{ji}. The node v_i has four neighboring pixels, four outward edges e_{ij} and four inward edges e_{ji}. For each edge e_{ij} or e_{ji}, the left pixel p is assumed to be "inside" while the right pixel q is assumed to be "outside". In order to accurately detect the interface between different retinal layers, the weighting function for the edge e_{ij}

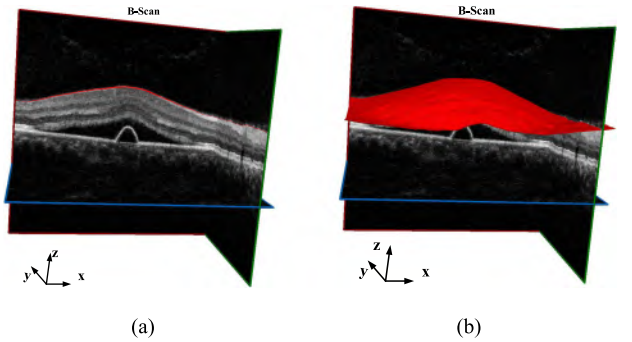

Fig. 6. Retinal surface detection. (a) Retinal layer boundaries with OCT volume; (b) Retinal surface detected by using the live wire algorithm with OCT volume.

is constructed as

$$c_{ij}(p,q) = \frac{\sum_{k=1}^{n_k}\sum_{l=1}^{n_l}\omega_k c_k\left(f_l(p,q)\right)}{\sum_{k=1}^{n_k}\omega_k}, \tag{7}$$

where f_l is the feature function, which define the edge feature for e_{ij}. The edge features consist of $n_l = 7$ features [32]: the pixel value of the left pixel p, the pixel value of the right pixel q, four gradient magnitudes and orientation-sensitive gradient magnitude. c_k is the transfer function, which maps an edge feature to the feature cost. The transfer functions consist of $n_k = 6$ functions [32]. ω_k is a positive constant indicating the emphasis given to feature f_l and transfer function c_k. Parameter training and the orientation property in the live wire algorithm allow it to find a proper boundary with the similar intensities and feature distributions of neighboring pixels/voxels. For the first slice in x-z plane (B-Scan) and in y-z plane, the corresponding transfer functions c_f and oriented edge features f_l are off-line trained and selected for each surface using a training image as described in [32], and those parameters of the next slice are online computed from the former slice. ω_k is also online computed. Since the values of transfer function can be normalized to $[0,\ 1]$, ω_k is set to 1.0 when the transfer function c_k is selected; while ω_k is set to 0 when the transfer function c_k is not selected in the implementation.

2) Surface 1 Detection: Live wire for single surface detection is proposed as shown in Fig. 6. The smoothed image is defined as a 3-D grid $\vec{x}$ with size $X \times Y \times Z$, where $\vec{x} = (x, y, z)$, $x = 1, 2, \ldots, X$, $y = 1, 2, \ldots, Y$ and $z = 1, 2, \ldots, Z$. The surface is defined as terrain-like interface $S(x, y) \in \{1, 2, \ldots, Z\}$, where each point (x, y) has one and only one $z \in \{1, 2, \ldots, Z\}$ value. Surface 1 detection is done by finding an oriented path with the minimum cost in $x - z$ plane and $y - z$ plane successively with an initial surface. Take $x - z$ plane (B-scan) as an instance, the initial anchors are equidistantly sampled in one direction with the sampling step lw_s from the initial curve. To search the shortest oriented path between two successive anchors, a graph is constructed and edge weights are computed as (7). The shortest oriented path $\langle e_1, e_2, \ldots, e_{n_o}\rangle$ is found. n_o is the number of edges on the shortest oriented path between two

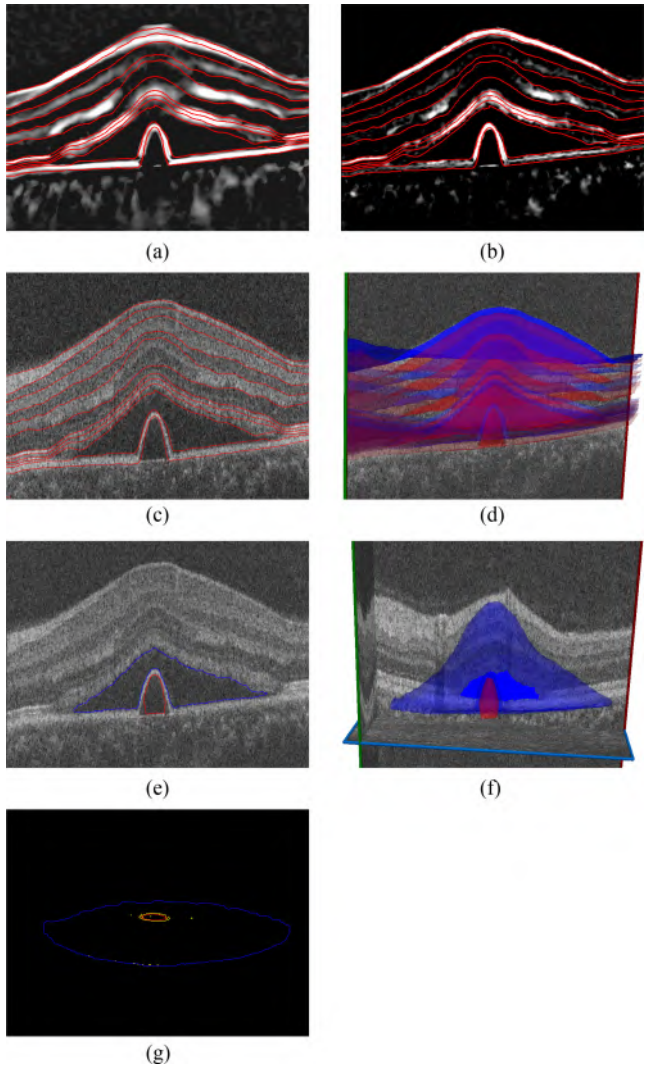

Fig. 7. Automatic surface detection and fluid segmentation. (a) Surfaces detected by proposed method and the bright layer response image ($\sigma_{t,\max} = 4.0$); (b) Surfaces detected by proposed method and the bright layer response image ($\sigma_{t,\max} = 2.0$); (c) Surfaces detected by proposed method and the original image; (d) 3D visualization of surfaces and the original image; (e) Fluid segmented by proposed method and the original image; (f) 3D visualization of fluid surfaces and the original image; (g) The blue curve indicates the footprint of the above surface of the segmented fluid, the yellow curves indicate the coarse footprint of pigment epithelial detachments and the red curve indicates the final fitted footprint of pigment epithelial detachments.

neighboring anchors $\mathbf{a}_o$ and $\mathbf{a}_{o+1}$. $o = 1, \ldots, \left\lfloor \frac{a_x}{lw_s} \right\rfloor$ and a_x is X in $x - z$ plane or Y in $y - z$ plane. The corresponding local energy can be defined as,

$$e_{lw}(\mathbf{a}_o, \mathbf{a}_{o+1}) = \sum_{u=1}^{n_o} c_{ij}(e_u) \tag{8}$$

Then, the total energy of a boundary curve can be defined as,

$$E_{lw} = \sum_{o=1}^{\left\lfloor \frac{a_x}{lw_s} \right\rfloor - 1} e_{lw}(\mathbf{a}_o, \mathbf{a}_{o+1}) \tag{9}$$

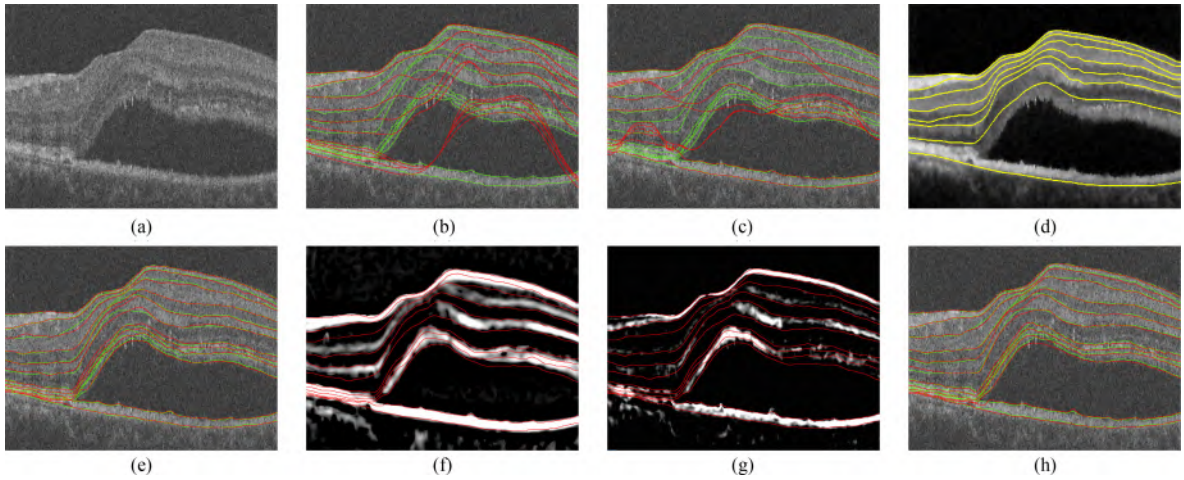

Fig. 8. Automatic surface detection (green curves indicate the segmentation reference, red curves indicate detected surfaces) of an OCT image with CSR. (a) The original image; (b) Surfaces detected via the IF algorithm; (c) Surfaces detected via the MGS algorithm; (d) The eight initial surfaces with the filtered image; (e) Surfaces detected via the RFSGLW algorithm; (f) Surfaces detected via the RFHLW algorithm and the bright layer response image ($\sigma_{t,\max} = 4.0$); (g) Surfaces detected via the RFHLW algorithm and the bright layer response image ($\sigma_{t,\max} = 2.0$); (h) Surfaces detected via the RFHLW algorithm.

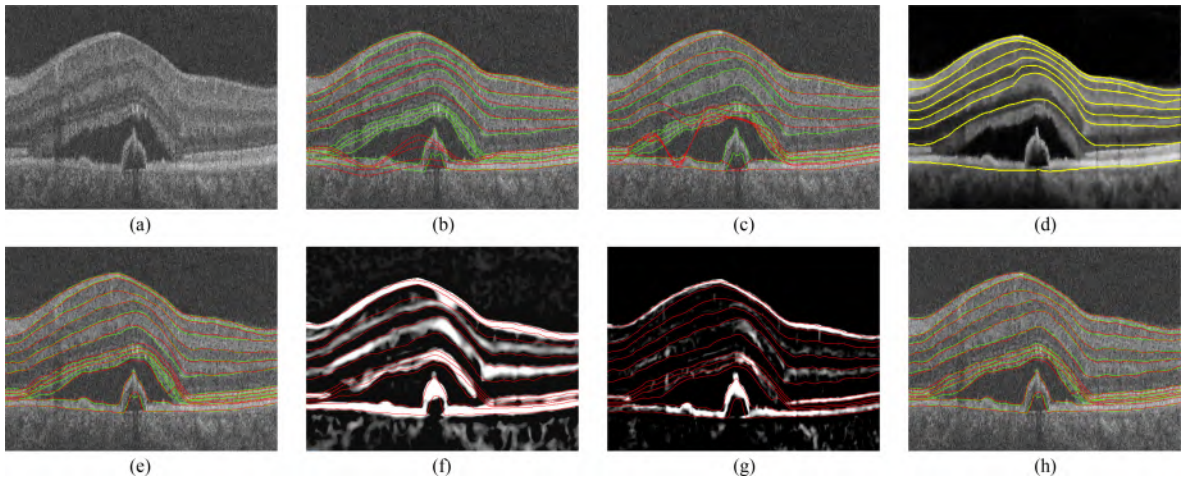

Fig. 9. Automatic surface detection (green curves indicate the segmentation reference, red curves indicate the detected surfaces) of an OCT image with CSR and pigment epithelial detachments. (a) The original image; (b) Surfaces detected via the IF algorithm; (c) Surfaces detected via the MGS algorithm; (d) The eight initial surfaces with the filtered image; (e) Surfaces detected via the RFSGLW algorithm; (f) Surfaces detected via the RFHLW algorithm and the bright layer response image ($\sigma_{t,\max} = 4.0$); (g) Surfaces detected via the RFHLW algorithm and the bright layer response image ($\sigma_{t,\max} = 2.0$); (h) Surfaces detected via the RFHLW algorithm.

Initial anchors $\mathbf{a}_o$ are equidistantly sampled with the step lw_s from the initial surfaces. The total energy of the refined boundary curve $\mathbf{a}'$ is computed according to (9). The step lw_s is reduced and $\mathbf{a}'$ is again considered as the initial curve. The process is stopped if the total energy difference between two iterations is not larger than ΔE or $lw_s \leq 1$. The procedure is shown in Algorithm 1. Due to the orientation of the live wire algorithm, the current slice image and the initial curve need to be flipped down before detect surface 1. The final curve needs to be flipped down after it is refined.

B. Hybrid Graph Live Wire

1) Hybrid Graph Construction: Most surfaces in OCT images are corrupted with speckles noise. The boundaries of the retinal layers are often blurred and of low contrast. Boundaries tends to be incorrectly detected via graph search algorithms [see Figs. 8(b)(c) and 9(b)(c)] and traditional live wire algorithm [see Figs. 8(e) and 9(e)]. To solve these problems, the anisotropic diffusion filtering [31] is first used to enhance the retinal layers and remove noise. In addition, our approach is based on a selective layer detection filter that avoids responses from non-layer structures and enhances layer structures. To accurately detect the boundary, a hybrid graph is constructed by integrating the filtered image and the bright layer enhanced image as shown in Fig. 5. Defining a special graph combining two graphs, or a hyper-graph, is a good choice to utilize the original information and the layer possibility information. Given two graphs $G^F = \left(V^F, E^F\right)$ for the filtered image and $G^B = \left(V^B, E^B\right)$ for the bright layer enhanced image, a special product graph is

defined as $G^H = \left(V^H, E^H\right)$, where, F stands for the filtered image, B stands for the layer enhanced image computed by (4) or (6), H stands for "hybrid". V^F and V^B are one-to-one corresponded. Instead of using a separate implementation of G^F and G^B, the product graph G^H is used to detect retinal surfaces. Since the critical points of total path cost are assumed to be minima, finding these minimal oriented edges yields the solution between two initial points. This requires an updated definition of the weight of the edge $c_{ij}\,(p,q)$ on the graph G. The edge weight of the product graph G^H is defined as

$$c_{ij}^H\,(p,q) = c_{ij}^F\,(p,q) \otimes c_{ij}^B\,(p,q), \tag{10}$$

where $\otimes$ denotes direct product, $c_{ij}^F\,(p,q)$ is the filtered image, $c_{ij}^B\,(p,q)$ is computed as (7) according to a layer enhanced image. Due to the underlying unifying property, the co-detection framework is not restricted to find the minimal cost path from only two images. It can be used to co-detect boundaries from multiple imaging modalities as long as the graph has the one-to-one correspondence property.

2) Surface Detection: Like Section VI-A2, the shortest oriented path $\langle e_1, e_2, \ldots, e_{n_o}\rangle$ is also found between two initial anchors. The corresponding local energy can be defined as,

$$e_{lw}^H\,(\mathbf{a}_o, \mathbf{a}_{o+1}) = \sum_{u=1}^{n_o} c_{ij}^H\,(e_u) \tag{11}$$

Then, the total energy of a boundary curve can be defined as,

$$E_{lw}^H = \sum_{o=1}^{\left\lfloor \frac{a_x}{lw_s} \right\rfloor - 1} e_{lw}^H\,(\mathbf{a}_o, \mathbf{a}_{o+1}) \tag{12}$$

The retinal surface is detected by the hybrid graph live wire algorithm as pseudo 3D terrain-like mesh. The hybrid live wire algorithm are employed in $x-z$ plane and then in $y-z$ plane. Combined with the above hybrid graph live wire refinement method for terrain-like surface detection, our optimization method is as Algorithm 1.

Algorithm 1: Live Wire for Retinal Surface Detection.

Require: The filtered and flattened image, $\bar{I}_f\,(\vec{x})$; The multiscale layer response, $L_m\,(\vec{x}, \sigma_t)$; The trained transfer functions, c_f; The trained edge features, f_l; The initial curve, $\mathbf{a}$; The sampling step, lw_s; The A-line flipping parameter, is_f; Energy parameter, ΔE.

Ensure: Energy parameter, E_{lw}; Updated curve, $\mathbf{a}'$; The updated transfer functions, c_f'; The updated edge features, f_l'.

```
Extract a 2D slice image from Ī_f(x⃗) and L_m(x⃗, σ_t) respectively;
if is_f = true then
    Flip the 2D slice image in z direction and the initial curve a;
end if
Construct a graph G;
Compute and assign the edge weight with the trained transfer functions c_f and the trained edge features f_l;
Consider the initial curve a as a';
E' ← ∞, E_lw ← 0;
while |E_lw − E'| > ΔE and lw_s > 1 do
    E' ← E_lw, E_lw ← 0;
    Sampling anchors a_o from the initial curve a' with the step lw_s;
    for Each two successive anchors a_o and a_{o+1} do
        Find the shortest oriented path ⟨e_1, e_2, ..., e_{n_o}⟩;
        Compute the local oriented boundary energy e_lw;
        E_lw ← E_lw + e_lw;
        Equidistantly find lw_s pixels as the oriented boundary along the oriented path and update a';
    end for
    lw_s ← lw_s/2.
end while
Smooth the final oriented path a'.
if is_f = true then
    Flip the final oriented path a' in z direction;
end if
Automatically train and select the transfer functions c_f' and the edge features f_l' according to the final oriented path a' for the 2D slice image of Ī_f(x⃗) and L_m(x⃗, σ_t) respectively as described in [32].
```

C. Layer and Fluid Segmentation

1) Surfaces 2-11 Detection: For the first slice of the bright layer enhanced image and the filtered image in x-z plane (B-Scan) and in y-z plane, the corresponding transfer functions c_f and the corresponding oriented edge features f_l are off-line trained and selected for each surface as described in [32], and those parameters of the next slice is online computed from the former slice. ω_k is also online computed. For the bright layer enhanced image and the filtered image respectively, ω_k is set to 1.0 when the transfer function c_k is selected; while ω_k is set to 0 when the transfer function c_k is not selected in the implementation. After finding the final oriented path $\mathbf{a}'$, c_f and f_l are trained and selected for the next slice. The orientation property favors boundary detection on a single orientation, i.e., the left pixel p of an edge e_{ji} is assumed to be "inside" while the right pixel q of the edge e_{ji} is assumed to be "outside". As can be seen in x-z plane [Fig. 5(c)], the oriented boundary (2D) or the surface (3D) represents the transition of a brighter layer to a darker layer from top to bottom. Surfaces 3, 5, 7, 9 and 11 have the dark-to-bright transition from top to bottom in the x-z plane or the y-z plane, while surfaces 2, 4, 6, 8 and 10 have the bright-to-dark transition. The darker layer is assumed to be "inside" while the brighter layer is assumed to be "outside". Therefore, to detect surfaces 3, 5, 7, 9 and 11, the 2D slice image and the initial curve $\mathbf{a}$ need to be flipped before the hybrid graph G^H is constructed and the anchors $\mathbf{a}_o$ are sampled.

2) Fluid Segmentation: After surface 7 is refined, fluid is segmented via thresholding constrained between surface 7 and the initial surface 8. The footprint of fluid is computed to label the disease region. The image under surface 7 is flattened again. A smaller scale bright layer detection filter is used to enhance the ellipsoid zone, the interdigitation zone and the RPE/Bruch's

complex layer, and suppress the OPSL, the dark layer between the interdigitation zone and the RPE/Bruch's complex layer, choroid and fluid. The initial surfaces 8–10 are successively obtained by the above surface and refined. In some cases as shown in Fig. 7, fluid may be associated with PEDs. The RPE layer may be locally deformed upwards under serosity. This deformation leads to inaccurate detection of surface 10 and surface 11. To refine these two surfaces, PEDs must be detected. Fluid above PEDs is first extracted from the segmented fluid. From surface 9 to surface 11, each A-line is scanned to find the above surface of the segmented fluid [the region within the blue curve in Fig. 7(g)] and stopped at the position of non-fluid to find the bottom surface. The two surfaces are coarsely considered as the hulls of fluid above PEDs. Similarly, from surface 11 to surface 9, each A-line is scanned to find the bottom surface of the segmented fluid and stopped at the position of non-fluid to find the above surface. These two surfaces are coarsely considered as the hulls of PED caused fluid. The footprint of the deformed RPE layer is then obtained in x-y plane. The pixel is considered in the footprint [the region within the yellow curve in Fig. 7(g)] if the distance between the top hulls of fluid above PEDs and PEDs caused fluid is larger than a given threshold value (four-voxel height) and the the distance between the bottom hull of fluid above PEDs and the above hull of PEDs caused fluid is larger than a given threshold value (four-voxel height). Morphological opening and closing are applied to the footprint. For each region in the footprint, the corresponding outer contour is computed via the convex hull algorithm [34] and is fitted as the corresponding ellipse. The fitted ellipses are considered as the footprint of PEDs [the region within the red curve in Fig. 7(g)]. Surface 10' is then adjusted according to the top hull of fluid above PEDs. Surface 11 is also generated based on the top hull of PEDs caused fluid. The final curves/surfaces are shown in Fig. 7(c)–(d). The segmented fluid is shown in Fig. 7(e)–(f).

VII. Experimental Evaluation

A. Data

The OCT images were obtained from Jiangsu Province Hospital by using a Cirrus HD-OCT 4000 scanner. Macula-centered SD-OCT scans of 48 eyes diagnosed with CSR were acquired as testing images. Another 6 macula-centered SD-OCT images with CSR were used as training images. All the OCT volume images contain $512 \times 128 \times 1024$ voxels and the voxel size is $11.74 \times 47.24 \times 1.96\ \mu\text{m}^3$.

B. Evaluation

To evaluate layer segmentation results, retinal specialists manually annotated surfaces in the B-scan images to form segmentation reference. Due to time consumption of manual annotation, only 15 out of the 128 B-scans were randomly chosen and annotated for each 3D OCT volume in the testing data set. All the 128 B-scans were manually annotated for each 3D OCT volume in the training data set, and then each 3D OCT volume was labeled with eight classes. To evaluate fluid segmentation results, fluid was also manually annotated for each 3D OCT volume in the testing data set. All fluid in the 128 B-scans was annotated slice by slice. This study was approved by the intuitional review board of Jiangsu Province Hospital and adhered to the tenets of the Declaration of Helsinki.

To evaluate performance of surface detection methods, average unsigned surface distance was computed for each surface by measuring absolute Euclidean distances in the z-axis between surface detection results of the algorithms and the reference surface. The average signed surface distance errors were computed for each surface by measuring distances in the z-axis between surface detection results of the algorithms and the reference surface [9]. To evaluate performance of fluid segmentation methods, we used three measures: true positive fraction (TPF), false positive fraction (FPF) and Dice similarity coefficient (DSC) defined as follows,

$$TPF = \frac{|F_r \cap F_a|}{|F_r|}, \tag{13}$$

$$FPF = \frac{|F_r \cap F_a|}{|B_r|}, \tag{14}$$

$$DSC = \frac{2\,|F_r \cap F_a|}{|F_r| + |F_a|}, \tag{15}$$

where $|\cdot|$ denotes the number of voxels; F_r denotes voxels manually annotated as fluid; F_a denotes voxels segmented as fluid via algorithms; B_r denotes voxels manually annotated as non-fluid. To demonstrate the improvement of our method, our random forest + hybrid live wire algorithm (RFHLW) was compared with the state-of-art methods: the Iowa reference algorithm (IR) [35], the multi-resolution graph search algorithm (MGS) [9], the Graph-Search-Graph-Cut algorithm (GSGC) [11] and random forest + single graph based live wire algorithm (RFSGLW). Paired t-tests were used to compare the surface detection and fluid segmentation errors and a p-value less than 0.05 was considered statistically significant.

C. Parameter Selection

Variance of the Gaussian smoothing filter was set to 2, the mean value was set to 0 and its kernel width was set to 9. Variance of the Canny edge detection algorithm was set 0.1, and its lower threshold and higher threshold were set the 0.02 and 0.15 of the maximal value of the Gaussian smoothed OCT image. The intensities of all features were mapped to $[0, 255]$, i.e., $I_{N,\max} = 255$. When smoothing by the curvature anisotropic diffusion filter, the conductance parameter λ_a was set to 3, the time step t_a was 0.06, the number of iterations n_a was typically set to 20. The filtered image within the interval $[25, 255]$ was transformed into $[0, 255]$. Five normalized features were generated from the filtered image within the intervals $[50, 170]$, $[55, 175]$, $[60, 180]$, $[65, 185]$ and $[70, 190]$. To compute layer responses, α and β were set to 0.25, the minimal scale $\sigma_{t,\min}$ was set to 2.0, the maximal scale scale $\sigma_{t,\max}$ was set to 5.0, and the scale step was set to 1.0. The number of random trees was set to 100, and the maximal depth of a tree was set to 10 for random forest training. For the refinement of surface 3–6, α and β were set to 0.25, the minimal scale $\sigma_{t,\min}$

TABLE I
COMPARISON OF SURFACE DETECTION WITH AVERAGE UNSIGNED SURFACE DISTANCE (MEAN ± SD μm[§]) FOR CSR IMAGES

Surface	IR	MGS	RFSGLW	RFHLW
1	12.23 ± 20.86	3.69 ± 5.49	2.59 ± 0.76	2.59 ± 0.76
2	21.43 ± 24.2	8.29 ± 15.81	4.83 ± 1.00	4.83 ± 1.00
3	25.61 ± 22.96	16.62 ± 16.13	4.87 ± 1.18	3.48 ± 0.74
4	24.81 ± 21.19	14.03 ± 15.71	2.75 ± 1.18	4.14 ± 1.34
5	27.81 ± 19.2	24.21 ± 18.91	4.79 ± 1.24	3.21 ± 1.73
6	29.78 ± 17.34	24.21 ± 15.44	6.36 ± 2.42	4.98 ± 1.73
7	56.89 ± 42.86	18.09 ± 15.65	8.77 ± 4.31	4.72 ± 1.62
8	53.74 ± 40.05	16.68 ± 13.17	9.52 ± 4.89	4.20 ± 1.98
9	52.5 ± 37.21	16.92 ± 11.33	10.95 ± 4.83	5.50 ± 2.77
10	29.55 ± 35.59	14.64 ± 10.17	8.27 ± 3.02	6.07 ± 2.81
10'	\	14.74 ± 25.38	6.64 ± 4.37	4.58 ± 3.46
11	26.62 ± 38.76	11.77 ± 28.51	3.54 ± 4.91	3.92 ± 3.92

§ Voxel size in z direction is 1.96 μm.

TABLE III
COMPARISON OF SURFACE DETECTION WITH AVERAGE SIGNED SURFACE DISTANCE (MEAN ± SD μm[§]) FOR CSR IMAGES

Surface	IR	MGS	RFSGLW	RFHLW
1	8.58 ± 21.13	-3.52 ± 5.49	1.68 ± 0.55	1.68 ± 0.55
2	15.54 ± 24.59	1.03 ± 7.00	4.40 ± 0.87	4.40 ± 0.87
3	20.29 ± 23.23	10.62 ± 8.15	0.13 ± 2.15	1.64 ± 1.02
4	13.04 ± 22.57	-1.86 ± 6.81	0.82 ± 1.81	3.53 ± 1.62
5	19.27 ± 19.67	17.77 ± 11.39	3.38 ± 2.10	2.26 ± 2.01
6	15.98 ± 19.19	9.60 ± 12.20	-2.88 ± 2.9	2.80 ± 1.78
7	53.67 ± 43.05	12.02 ± 13.96	-1.6 ± 5.09	2.64 ± 2.00
8	45.54 ± 41.18	3.90 ± 12.46	-5.25 ± 5.44	0.20 ± 2.75
9	38.65 ± 39.87	-1.51 ± 11.59	-7.09 ± 5.65	1.78 ± 3.55
10	-14.30 ± 40.18	-5.27 ± 10.71	-1.47 ± 4.96	3.25 ± 4.01
10'	\	-11.81 ± 26.12	-6.12 ± 4.48	-1.15 ± 3.95
11	-12.71 ± 42.57	-9.53 ± 29.05	-1.01 ± 5.34	1.34 ± 4.44

§ Voxel size in z direction is 1.96 μm.

TABLE II
P-VALUES OF AVERAGE UNSIGNED SURFACE DISTANCE FOR CSR IMAGES

Surface	RFHLW vs IR	RFHLW vs MGS	RFHLW vs RFSGLW
1	0.0028	0.1862	\
2	1.99×10^{-5}	0.1403	\
3	3.12×10^{-8}	1.22×10^{-6}	1.02×10^{-10}
4	1.85×10^{-8}	7.20×10^{-5}	3.00×10^{-11}
5	8.43×10^{-12}	6.12×10^{-10}	7.89×10^{-10}
6	5.34×10^{-13}	5.31×10^{-4}	2.68×10^{-5}
7	6.85×10^{-11}	5.80×10^{-5}	2.28×10^{-9}
8	4.37×10^{-11}	0.0634	2.91×10^{-11}
9	2.09×10^{-11}	0.0767	1.76×10^{-10}
10	2.57×10^{-5}	4.41×10^{-8}	1.62×10^{-6}
10'	\	0.0094	2.12×10^{-5}
11	3.21×10^{-4}	0.0680	0.4175

TABLE IV
P-VALUES OF AVERAGE SIGNED SURFACE DISTANCE FOR CSR IMAGES

Surface	RFHLW vs IR	RFHLW vs MGS	RFHLW vs RFSGLW
1	0.0324	4.91×10^{-8}	\
2	0.0033	8.77×10^{-4}	\
3	1.80×10^{-6}	1.51×10^{-9}	8.70×10^{-8}
4	0.0052	5.56×10^{-7}	5.06×10^{-16}
5	1.70×10^{-7}	2.31×10^{-13}	0.0015
6	2.87×10^{-5}	4.94×10^{-11}	9.65×10^{23}
7	1.65×10^{-10}	2.48×10^{-7}	6.31×10^{-9}
8	1.80×10^{-9}	1.69×10^{-8}	9.69×10^{-12}
9	6.77×10^{-8}	1.91×10^{-9}	1.32×10^{-18}
10	0.0055	7.29×10^{-6}	3.78×10^{-15}
10'	\	0.0066	1.75×10^{-14}
11	0.0685	0.0160	1.16×10^{-4}

was set to 2.0, the maximal scale scale $\sigma_{t,\max}$ was set to 4.0, and the scale step was set to 1.0. For the refinement of surface 7–11, α and β were set to 0.25, only one scale $\sigma_t = 2.0$ was used for the construction of the hybrid graph G^H. The initial step size lw_s was set to 1/15 of the width of the B-scan image or the y-z image and the single graph and hybrid live wire algorithm were stopped at $\Delta E^H = \Delta E = 3000$. The scale of the bright layer detection filter were set to 2.0 for the refinement of surface 7–11. The connected threshold was set to 45 in order to refine surface 6, 7. The threshold for fluid segmentation was also set to 45.

VIII. EXPERIMENTAL RESULTS

A. Surface Detection Results

An OCT volume image only with CSR is shown in Fig. 8. Another OCT volume with CSR and PEDs is shown in Fig. 9. The green curves indicate manual annotated surfaces. The red curves indicate the detected surfaces via the surface detection algorithms. The yellow curves indicate the eight initial surfaces by using the modified random forest method. Table I shows the mean and standard deviation of average unsigned surface detection errors for each surface. The p-values of average unsigned surface detection errors for each surface are shown in Table II. Table III shows the mean and standard deviation of average signed surface detection errors for each surface. The p-values of average signed surface detection errors for each surface are shown in Table IV.

For the IR algorithm [35], the average unsigned surface detection errors of surface 1 to 11 were significantly large as shown in the first colum of Table I, and surface detection errors were the largest at surface 7 to 9 while detection errors of the rest surfaces were slightly smaller. As can be seen in the first column of Table III, the average signed surface detection errors of surface 1 to 9 were positive and large and the average signed surface detection errors were also the largest at surface 7 to 9. These surface detection errors showed the mean position of the detected surface 1 to 9 via the IR algorithm were lower than that of the segmentation reference while the mean position of surface 10 to 11 were higher. These surface detection errors were consistent with surface detection results shown in Figs. 8(b) and 9(b). Surface detection error occurred from surface 2 to surface 11 where the large serosity made layers were deformed upwards. For the MGS algorithm [9], the average unsigned surface detection errors of surface 1 to 11 were slightly smaller than the IR algorithm as shown in the second column of Table I. Surface detection errors were the largest at surface 5 to 7 while detection errors of the rest surfaces were slightly smaller.

TABLE V
COMPARISON OF FLUID SEGMENTATION (MEAN ± SD %)

	TPF	FPF	DSC
IR	9.04 ± 11.84	0.01 ± 0.03	14.65 ± 15.06
GSGC	64.67 ± 28.96	0.05 ± 0.07	71.05 ± 30.32
MGS	80.19 ± 21.76	0.18 ± 0.18	74.58 ± 20.56
RFSGLW	84.52 ± 20.53	0.03 ± 0.07	88.33 ± 19.68
RFHLW	92.73 ± 15.03	0.05 ± 0.09	92.73 ± 14.21

As can be seen in the second column of Table III, the average signed surface detection errors of surface 5 to 7 were positive and large and the average signed surface detection errors were also the largest at surface 5 to 7. As shown in Figs. 8(c) and 9(c), surface detection error occurred from surface 2 to surface 11 also due to the appearance of the serosity. The surface detection via the MGS algorithm for OCT images with pigment epithelial detachments first segmented surface 7; however, the bottom surface of serosity tended to be detected incorrectly as surface 7. Surface 2 to 6 were refined with surface 7; therefore, the average surface detection errors of surface 5 to 7 were large as s shown in Figs. 8(c) and 9(c).

The results in Tables I and III show great improvement over the IR algorithm [35] and the MGS algorithm [9] even a large proportion of the layers exhibits dramatic morphological changes. For the RFSGLW algorithm, the average unsigned surface detection errors of surface 1 to 11 were dramatically reduced compared to the IR algorithm and the MGS algorithm as shown in the third column of Table I. Surface detection errors were the largest at surface 5 to 7 while detection errors of the rest surfaces were smaller. As can be seen in the third column of Table III, the average signed surface detection errors of surface 6 to 11 were negative. It means the mean positions of the detected surface 6 to 11 via the RFSGLW algorithm were higher than those of the segmentation reference. For surface 6, the occurrence of serosity lead to low intensity of OPL above the abnormal region as shown in Figs. 1, 8 and 9. As can be seen in Figs. 8(e) and 9(e), the detected surface 6 was in the internal of the OPL. For surface 7–11, the average signed surface detection errors disturbed by ELM can be seen Figs. 8(e) and (e). However, ellipsoid zone was higher enhanced via the bright layer detection filter with a large scale while the bright layer response of ELM was much weaker as shown in Figs. 8(f) and 9(f) . Compared to the RFSGLW algorithm, the RFHLW algorithm improved the detection of surface 7 as shown in Figs. 8(h) and 9(h).

B. Fluid Segmentation Results

An example of fluid segmentation result of an OCT image only with CSR is shown in Fig. 10 and another example with CSR and pigment epithelial detachments is shown in Fig. 11. The green curves indicate manually annotated fluid. The red curves indicate the segmented fluid via the fluid segmentation algorithm. Table V shows the mean and standard deviation of TPF, FPF and DSC. The p-values of the three evaluation measures for fluid segmentation are shown in Table VI.

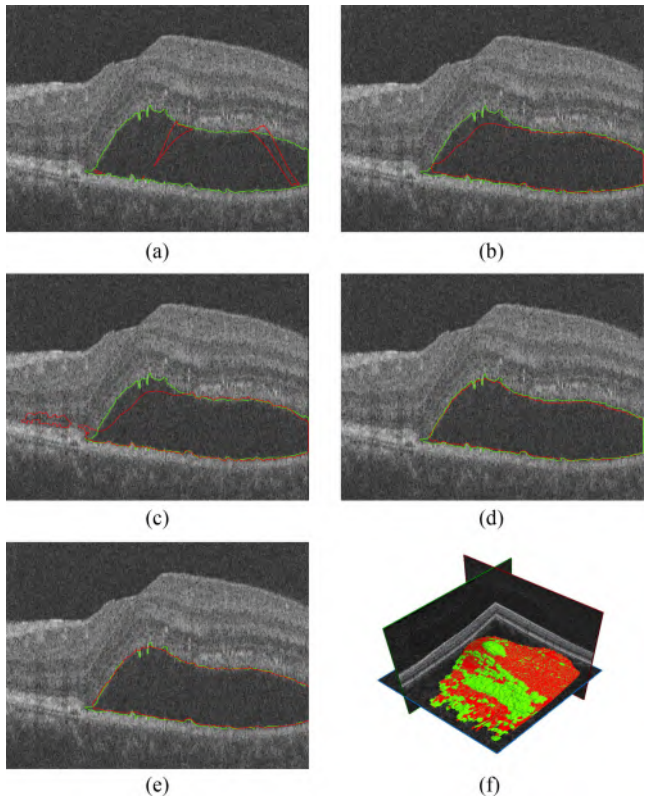

Fig. 10. Automatic fluid segmentation (green curves indicate the segmentation reference, red curves indicate the segmented fluid) of an OCT image with CSR. (a) Fluid segmented via the IF algorithm; (b) Fluid was segmented via the MGS algorithm; (c) Fluid segmented via the GSGC algorithm; (d) Fluid segmented via the RFSGLW algorithm; (e) Fluid segmented via the RFHLW algorithm; (f) 3D visualization of fluid segmented via the RFHLW algorithm (red) and manual annotation (green).

TABLE VI
P-VALUES OF FLUID SEGMENTATION

	TPF	FPF	DSC
RFHLW vs IR	1.47×10^{-32}	2.24×10^{-4}	1.69×10^{-29}
RFHLW vs GSGC	7.61×10^{-9}	0.4162	1.95×10^{-6}
RFHLW vs MGS	1.13×10^{-4}	7.74×10^{-8}	4.23×10^{-9}
RFHLW vs RFSGLW	0.0010	3.90×10^{-5}	0.0382

For the IR algorithm [35], the same threshold algorithm was employed to segment fluid on the same data. The fluid was segmented between surface 7, 11 detected via the IR algorithm. Because of the inaccurate surface detection, small region of fluid was obtained as shown in Figs. 10(a) and 11(a). This led to much lower values of TPF, FPF and DSC as shown in the first row of Table V. Since morphological changes are similar between CSR and the symptomatic exudate-associated derangement, the GSGC algorithm [11] was also tested on the same data. Surface 7 and surface 11 were used as the two constraining surfaces. However, the GSGC algorithm for fluid segmentation depends on the surface detection algorithm. As can be seen from the IR algorithm [35] and the MGS algorithm [9], the GS based surface detection algorithm is not robust to deformation of retinal layers, and thus slight improvement was achieved as shown in the second row of Table V. For the MGS algorithm [9], the same

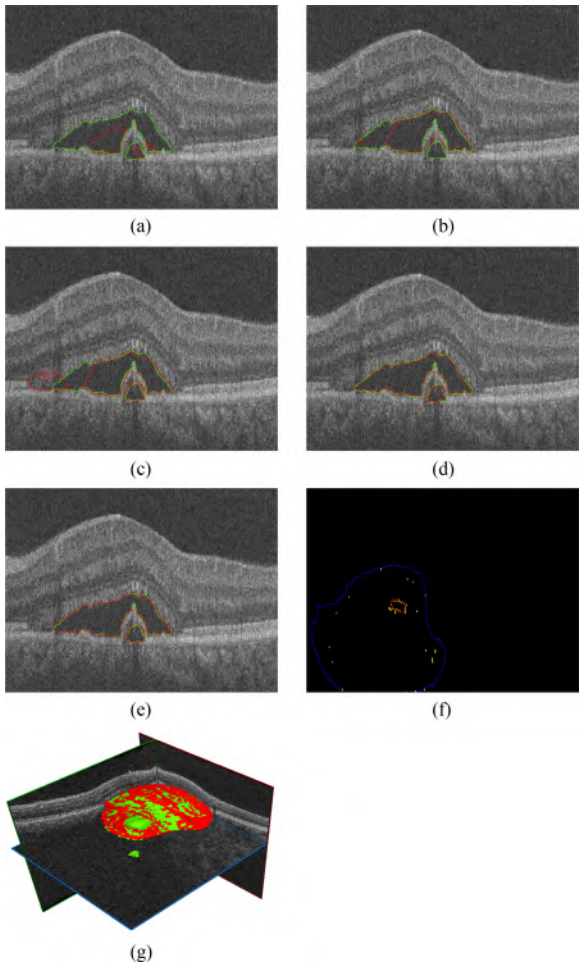

Fig. 11. Automatic fluid segmentation (green curves indicate the segmentation reference, red curves indicate the segmented fluid) of an OCT image with CSR and pigment epithelial detachments. (a) Fluid segmented via the IF algorithm; (b) Fluid segmented via the MGS algorithm; (c) Fluid segmented via the GSGC algorithm; (d) Fluid segmented via the RFSGLW algorithm; (e) Fluid segmented via the RFHLW algorithm; (f) 3D visualization of fluid segmented via the RFHLW algorithm (red) and manual annotation (green); (g) The blue curve indicates the footprint of the above surface of the segmented fluid, the yellow curves indicate the coarse footprint of pigment epithelial detachments and the red curve indicates the final fitted footprint of pigment epithelial detachments.

threshold algorithm was also used to segment fluid on the same data between surface 7 and surface 11. TPF was $80.19 \pm 21.76\%$ via the MGS algorithm; however, FPF also reached $0.18 \pm 0.18\%$ and DSC was only $74.58 \pm 20.56\%$. This is also because the MGS algorithm produced large surface detection errors of surface 7 and surface 11. Due to the inaccurate surface 7 detection, values of TPF and DSC were also smaller than the he RFHLW algorithm. As shown Table VI, the RFHLW algorithm achieved statistically different results compared to the IR algorithm [35], the GSGC algorithm [11], the MGS algorithm [9] and the RFSGLW algorithm.

C. Running Time

The proposed algorithm was implemented in C++ and tested on a PC with Intel i5-3450 CPU@3.10GHz and 16 GB of RAM. The average running time of the algorithm was 407 ± 54 s for CSR OCT images. The average running time of the IF algorithm was 103 ± 27 s for CSR OCT images. The average running time of the GSGC algorithm for region segmentation was 498 ± 51 s for CSR OCT images. The average running time of the MGS algorithm was 458 ± 141 s for CSR OCT images.

IX. Conclusion

In this paper, a supervised method is proposed for the automatic segmentation of retinal layers and fluid on OCT scans of eyes with CSR. After surface 1 is detected, the B-scan image is aligned and flattened. Only twenty four features are generated for the training and testing of random forests classifiers, and then eight initial surfaces are detected as constraints. By utilizing the original intensities of OCT images and the layer-like shape information, a hyper graph is constructed to find the minimal oriented path cost. Surfaces between neighboring layers are successively detected from surfaces 2 to 11 based on the hyper graph live wire algorithm. With the proper surface detection, fluid segmentation can be achieved by using a thresholding method. The proposed method can also cope with the OCT images with both central serous retinopathy and pigment epithelial detachments.

The proposed method is able to deal with abnormalities such as fluid and PEDs. For testing CSR images, surface detection errors were statistically significantly smaller than those of the state-of-art methods such as the IR algorithm [35] and the MGS algorithm [9]. Meanwhile, the RFHLW algorithm also outperformed the RFSGLW algorithm. This is because ellipsoid zone was higher enhanced via the bright layer detection filter while ELM was restrained. Simultaneous fluid segmentation was also achieved. The proposed method also achieved higher true positive fraction, higher Dice similarity coefficient and lower false positive fraction, which were statistically different from the results obtained by the IR algorithm [35], the MGS algorithm [9], the GSGC algorithm [11] and the RFSGLW algorithm. In summary, the proposed algorithm can be utilized for quantitative analysis of features of individual retinal layers for OCT images with CSR.

References

[1] G. Staurenghi, S. Sadda, U. Chakravarthy, and R. F. Spaide, "Proposed lexicon for anatomic landmarks in normal posterior segment spectral-domain optical coherence tomography: The IN-OCT consensus," *Ophthalmology*, vol. 121, no. 8, pp. 1572–1578, 2014.

[2] M. G. Field *et al.*, "Detection of retinal metabolic stress due to central serous retinopathy," *Retina*, vol. 29, no. 8, pp. 1162–1166, 2009.

[3] B. Hassan, G. Raja, T. Hassan, and M. U. Akram, "Structure tensor based automated detection of macular edema and central serous retinopathy using optical coherence tomography images," *J. Opt. Soc. Amer. A*, vol. 33, no. 4, pp. 455–463, 2016.

[4] H. Matsumoto, T. Sato, and S. Kishi, "Outer nuclear layer thickness at the fovea determines visual outcomes in resolved central serous chorioretinopathy," *Amer. J. Ophthalmol.*, vol. 148, no. 1, pp. 105–110, 2009.

[5] C. Ahlers, W. Geitzenauer, G. Stock, I. Golbaz, U. Schmidt-Erfurth, and C. Prünte, "Alterations of intraretinal layers in acute central serous chorioretinopathy," *Acta ophthalmologica*, vol. 87, no. 5, pp. 511–516, 2009.

[6] J. Novosel, Z. Wang, H. de Jong, M. van Velthoven, K. A. Vermeer, and L. J. van Vliet, "Locally-adaptive loosely-coupled level sets for retinal layer and fluid segmentation in subjects with central serous retinopathy," in *Proc. 2016 IEEE 13th Int. Symp. Biomed. Imag.*, 2016, pp. 702–705.

[7] C. Jin *et al.*, "3d fast automatic segmentation of kidney based on modified AAM and random forest," *IEEE Trans. Med. Imag.*, vol. 35, no. 6, pp. 1395–1407, Jun. 2016.
[8] M. Yaqub, M. K. Javaid, C. Cooper, and J. A. Noble, "Investigation of the role of feature selection and weighted voting in random forests for 3-d volumetric segmentation," *IEEE Trans. Med. Imag.*, vol. 33, no. 2, pp. 258–271, Feb. 2014.
[9] F. Shi *et al.*, "Automated 3-d retinal layer segmentation of macular optical coherence tomography images with serous pigment epithelial detachments," *IEEE Trans. Med. Imag.*, vol. 34, no. 2, pp. 441–452, Feb. 2015.
[10] A. Lang *et al.*, "Retinal layer segmentation of macular OCT images using boundary classification," *Biomed. Opt. Express*, vol. 4, no. 7, pp. 1133–1152, 2013.
[11] X. Chen, M. Niemeijer, L. Zhang, K. Lee, M. D. Abràmoff, and M. Sonka, "Three-dimensional segmentation of fluid-associated abnormalities in retinal OCT: Probability constrained graph-search-graph-cut," *IEEE Trans. Med. Imag.*, vol. 31, no. 8, pp. 1521–1531, Feb. 2012.
[12] M. K. Garvin, M. D. Abràmoff, R. Kardon, S. R. Russell, X. Wu, and M. Sonka, "Intraretinal layer segmentation of macular optical coherence tomography images using optimal 3-d graph search," *IEEE Trans. Med. Imag.*, vol. 27, no. 10, pp. 1495–1505, Oct. 2008.
[13] M. K. Garvin, M. D. Abramoff, X. Wu, S. R. Russell, T. L. Burns, and M. Sonka, "Automated 3-d intraretinal layer segmentation of macular spectral-domain optical coherence tomography images," *IEEE Trans. Med. Imag.*, vol. 28, no. 9, pp. 1436–1447, Sep. 2009.
[14] S. Lu, C. Y.-l. Cheung, J. Liu, J. H. Lim, C. K.-s. Leung, and T. Y. Wong, "Automated layer segmentation of optical coherence tomography images," *IEEE Trans. Biomed. Eng.*, vol. 57, no. 10, pp. 2605–2608, Oct. 2010.
[15] Q. Song, J. Bai, M. K. Garvin, M. Sonka, J. M. Buatti, and X. Wu, "Optimal multiple surface segmentation with shape and context priors," *IEEE Trans. Med. Imag.*, vol. 32, no. 2, pp. 376–386, Feb. 2013.
[16] Q. Yang *et al.*, "Automated layer segmentation of macular OCT images using dual-scale gradient information," *Opt. Express*, vol. 18, no. 20, pp. 21293–21307, 2010.
[17] R. Kafieh, H. Rabbani, M. D. Abramoff, and M. Sonka, "Intra-retinal layer segmentation of 3d optical coherence tomography using coarse grained diffusion map," *Med. Image Anal.*, vol. 17, no. 8, pp. 907–928, 2013.
[18] G. Li, X. Chen, F. Shi, W. Zhu, J. Tian, and D. Xiang, "Automatic liver segmentation based on shape constraints and deformable graph cut in CT images," *IEEE Trans. Image Process.*, vol. 24, no. 12, pp. 5315–5329, Dec. 2015.
[19] D. Xiang *et al.*, "Cortexpert: A model-based method for automatic renal cortex segmentation," *Med. Image Anal.*, vol. 42, pp. 257–273, 2017.
[20] J. Tian, B. Varga, G. M. Somfai, W.-H. Lee, W. E. Smiddy, and D. C. DeBuc, "Real-time automatic segmentation of optical coherence tomography volume data of the macular region," *PloS One*, vol. 10, no. 8, 2015, Art. no. e0133908.
[21] K. Vermeer, J. Van der Schoot, H. Lemij, and J. De Boer, "Automated segmentation by pixel classification of retinal layers in ophthalmic OCT images," *Biomed. Opt. Express*, vol. 2, no. 6, pp. 1743–1756, 2011.
[22] P. P. Srinivasan, S. J. Heflin, J. A. Izatt, V. Y. Arshavsky, and S. Farsiu, "Automatic segmentation of up to ten layer boundaries in SD-OCT images of the mouse retina with and without missing layers due to pathology," *Biomed. Opt. Express*, vol. 5, no. 2, pp. 348–365, 2014.
[23] J. Novosel, G. Thepass, H. G. Lemij, J. F. de Boer, K. A. Vermeer, and L. J. van Vliet, "Loosely coupled level sets for simultaneous 3d retinal layer segmentation in optical coherence tomography," *Med. Image Anal.*, vol. 26, no. 1, pp. 146–158, 2015.
[24] G. Quellec, K. Lee, M. Dolejsi, M. K. Garvin, M. D. Abramoff, and M. Sonka, "Three-dimensional analysis of retinal layer texture: Identification of fluid-filled regions in SD-OCT of the Macula," *IEEE Trans. Med. Imag.*, vol. 29, no. 6, pp. 1321–1330, Jun. 2010.
[25] P. A. Dufour *et al.*, "Graph-based multi-surface segmentation of OCT data using trained hard and soft constraints," *IEEE Trans. Med. Imag.*, vol. 32, no. 3, pp. 531–543, Mar. 2013.
[26] W. Ding *et al.*, "Automatic detection of subretinal fluid and sub-retinal pigment epithelium fluid in optical coherence tomography images," in *Proc. 2013 35th Annu. Int. Conf. IEEE Eng. Med. Biol. Soc.*, 2013, pp. 7388–7391.
[27] X. Xu, K. Lee, L. Zhang, M. Sonka, and M. D. Abràmoff, "Stratified sampling voxel classification for segmentation of intraretinal and subretinal fluid in longitudinal clinical OCT data," *IEEE Trans. Med. Imag.*, vol. 34, no. 7, pp. 1616–1623, Jul. 2015.
[28] J. Wang *et al.*, "Automated volumetric segmentation of retinal fluid on optical coherence tomography," *Biomed. Opt. Express*, vol. 7, no. 4, pp. 1577–1589, 2016.
[29] L. de Sisternes, G. Jonna, J. Moss, M. F. Marmor, T. Leng, and D. L. Rubin, "Automated intraretinal segmentation of SD-OCT images in normal and age-related macular degeneration eyes," *Biomed. Opt. Express*, vol. 8, no. 3, pp. 1926–1949, 2017.
[30] J. Novosel, K. A. Vermeer, J. H. de Jong, Z. Wang, and L. J. van Vliet, "Joint segmentation of retinal layers and focal lesions in 3-d OCT data of topologically disrupted retinas," *IEEE Trans. Med. Imag.*, vol. 36, no. 6, pp. 1276–1286, Jun. 2017.
[31] R. T. Whitaker and X. Xue, "Variable-conductance, level-set curvature for image denoising," in *Proc. 2001. Int. Conf. Image Process.,* 2001, vol. 3, pp. 142–145.
[32] A. X. Falcão, J. K. Udupa, S. Samarasekera, S. Sharma, B. E. Hirsch, and R. d. A. Lotufo, "User-steered image segmentation paradigms: Live wire and live lane," *Graphical Models Image Process.*, vol. 60, no. 4, pp. 233–260, 1998.
[33] A. X. Falcão and J. K. Udupa, "A 3d generalization of user-steered live-wire segmentation," *Med. Image Anal.*, vol. 4, no. 4, pp. 389–402, 2000.
[34] R. L. Graham and F. F. Yao, "Finding the convex hull of a simple polygon," *J. Algorithms*, vol. 4, no. 4, pp. 324–331, 1983.
[35] Iowa reference algorithms: Human and murine 3d OCT retinal layer analysis and display, Iowa Inst. Biomed. Imag., Iowa City, IA, USA. [Online]. Available: http://www.biomed-imaging.uiowa.edu/content/shared-software-download